Mean precipitation change from a deepening troposphere

Nadir Jeevanjee[a,b,c,1] **and David M. Romps**[d,e]

[a]Department of Geosciences, Princeton University, Princeton, NJ 08544; [b]Princeton Program in Atmosphere and Ocean Sciences, Princeton University, Princeton, NJ 08540; [c]Geophysical Fluid Dynamics Laboratory, Princeton, NJ 08540; [d]Department of Earth and Planetary Science, University of California, Berkeley, CA 94702; and [e]Climate and Ecosystems Sciences Division, Lawrence Berkeley National Laboratory, Berkeley, CA 94702

Edited by Kerry A. Emanuel, Massachusetts Institute of Technology, Cambridge, MA, and approved September 24, 2018 (received for review November 27, 2017)

Global climate models robustly predict that global mean precipitation should increase at roughly 2–3% K^{-1}, but the origin of these values is not well understood. Here we develop a simple theory to help explain these values. This theory combines the well-known radiative constraint on precipitation, which says that condensation heating from precipitation is balanced by the net radiative cooling of the free troposphere, with an invariance of radiative cooling profiles when expressed in temperature coordinates. These two constraints yield a picture in which mean precipitation is controlled primarily by the depth of the troposphere, when measured in temperature coordinates. We develop this theory in idealized simulations of radiative–convective equilibrium and also demonstrate its applicability to global climate models.

climate change | atmospheric sciences | hydrological cycle | atmospheric radiation

Despite its fundamental role in driving atmospheric motions, atmospheric radiative cooling remains somewhat enigmatic. Though the fundamentals of radiative transfer are well-understood, translating these fundamentals into realistic cooling rates requires complicated radiative transfer calculations that render the final result somewhat inscrutable. As a result, we lack simple descriptions of the radiative cooling profiles produced by our numerical models.

One implication is that quantities that are closely tied to radiative cooling, such as global mean precipitation, also remain somewhat enigmatic. We do know that the atmospheric (rather than planetary) energy budget, in which condensation heating from precipitation balances atmospheric radiative cooling, constrains global mean precipitation P to be roughly equal to column-integrated net radiative cooling Q_{net} (1–3):

$$LP \approx Q_{\text{net}} \quad (\text{W/m}^2) \qquad [1]$$

(here L is the latent heat of vaporization, and we neglect surface sensible heat fluxes, a point we return to below). We also know that global climate models (GCMs) robustly exhibit increases in P with warming of $2-3\%\ \text{K}^{-1}$ (4–6). Furthermore, recent work has attributed this increase to an increase in downward radiative emission from the atmosphere at the surface (7–9). Despite this progress, however, a basic question remains unanswered: Why does this increase take on the value that it does? Why $2-3\%\ \text{K}^{-1}$ and not many times larger or smaller?

This paper aims to reveal some simple behavior in radiative cooling profiles and to use it to answer this question about precipitation change. We will focus on how vertically resolved radiative cooling profiles change with warming, rather than focusing on radiative fluxes at the surface or top-of-atmosphere. In particular, we will argue, following refs. 10, 11, that water vapor density and optical depth profiles should behave simply when considered as functions of temperature as a vertical coordinate. This implies that longwave (LW) and shortwave (SW) radiative flux divergences should also behave simply in temperature coordinates. This simple behavior leads to a predictive expression for $dQ_{\text{net}}/dT_{\text{s}}$ and hence dP/dT_{s} (T_{s} is surface temperature), which we validate with limited-area cloud-resolving model (CRM) simulations that emulate the tropical atmosphere. We then seek insight from our results and also apply them to GCMs.

This approach leverages the insights of refs. 10, 11 but also builds upon their work in various ways. First, we verify some of their ideas using comprehensive radiative transfer calculations, which to our knowledge has not yet been done. We also shift the focus from outgoing LW radiation (i.e., thermal emission to space) to atmospheric radiative cooling, and also extend their arguments to include both the LW (thermal emission) and SW (solar radiation) bands. Our work also has precedent in ref. 9, which similarly takes an idealized approach in analyzing the radiative constraint on hydrological sensitivity. That study, however, used a gray radiation model wherein the concentration of the LW absorber is not directly tied to temperature, a link that will prove crucial here (see Eqs. **2**–**4** below).

CRM Simulations of RCE

We begin by studying precipitation change in one of the simplest systems in which the radiative constraint on precipitation (Eq. **1**) operates, namely cloud-resolving radiative–convective equilibrium (RCE). This system is an idealized and isolated version of Earth's tropics and exhibits precipitation increases of roughly $3-4\%\ \text{K}^{-1}$, similar to the GCM range (12, 13).

We simulate RCE using Das Atmosphärische Modell (DAM) (14), a fully compressible, nonhydrostatic CRM, coupled to radiation via the comprehensive Rapid Radiative Transfer Model (RRTM) (15). DAM used the six-class Lin–Lord–Krueger

Significance

Global climate models robustly predict that global mean precipitation should increase at roughly 2–3% K^{-1}, but the origin of these values is not well understood. Here we develop a simple theory to help explain these values. This theory suggests that global mean precipitation is closely tied to the depth of the troposphere, when measured in temperature coordinates. When surface temperatures increase, this "temperature depth" of the troposphere also increases, causing an increase in global mean precipitation.

Author contributions: N.J. designed research; N.J. and D.M.R. performed research; N.J. and D.M.R. analyzed data; and N.J. wrote the paper.

The authors declare no conflict of interest.

This article is a PNAS Direct Submission.

[1]To whom correspondence should be addressed. Email: nadirj@princeton.edu.

This article contains supporting information online at www.pnas.org/lookup/suppl/doi:10.1073/pnas.1720683115/-/DCSupplemental.

microphysics scheme (16–18) and in contrast to its original formulation in ref. 14 uses no explicit subgrid scale turbulence scheme, relying instead on "implicit large-eddy simulation" (19) (essentially just the existing numerical diffusion) for subgrid scale transport.

Our RCE simulations ran on a square doubly periodic domain of horizontal dimension $L = 72$ km, with a horizontal grid spacing of $dx = 1$ km. The vertical grid spacing stretched smoothly from 50 m below 1,000 m to 250 m between 1,000 m and 5,000 m and then to 500 m up to the model top at 30 km. We calculated surface heat and moisture fluxes using simple bulk aerodynamic formulae and used a preindustrial CO_2 concentration of 280 ppm with no ozone. To explore precipitation changes with warming, we ran five experiments at prescribed surface temperatures of $T_s = (280, 290, 300, 310, 320)$ K, though some of our figures omit the 320 K run for clarity. Our runs branched off the equilibrated runs described in ref. 20 and were run for 60 d to iron out any artifacts from changing the domain and resolution. All vertical profiles are time mean and domain mean, averaged over the last 20 d of each run. These simulations do not exhibit any organization or "self-aggregation" (21) (*SI Appendix*, Fig. S1).

Since we run with prescribed T_s and fixed CO_2, we are isolating the hydrological sensitivity to T_s and neglecting the rapid adjustment from CO_2. The former is relatively robust across models and forcing types, whereas rapid adjustments depend on forcing type (22, 23). The latter contributes roughly -0.5 $W/m^2/K$ in $4 \times CO_2$ experiments (22), a nondominant effect.

T_s Invariance of Flux Divergences

The simple behavior of radiative cooling alluded to above begins with the key fact that the water vapor density

$$\rho_v = \mathrm{RH}\frac{p_v^*(T)}{R_v T} \qquad [2]$$

is (up to variations in relative humidity RH) a function of temperature only. [Note that it has been shown recently that RH is itself a function of T in RCE (20). Also, here p_v^* is the saturation vapor pressure of water, and all other symbols have their usual meaning.] If we use T as a vertical coordinate, Eq. **2** then tells us that the function $\rho_v(T)$ does not depend on T_s. This is what we mean by "T_s invariance." We verify the T_s invariance of $\rho_v(T)$ in our simulations in Fig. 1, where indeed the ρ_v profiles at different T_s collapse onto a single curve when plotted in temperature coordinates.

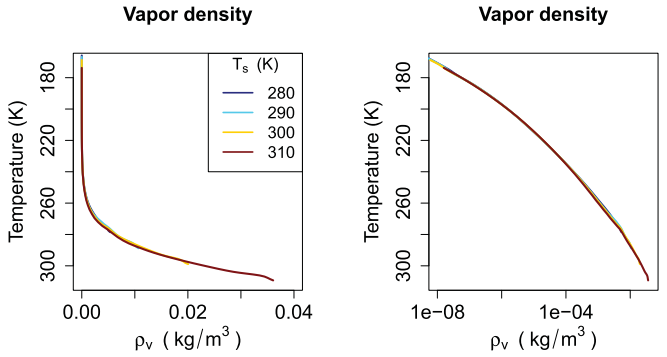

Fig. 1. Profiles of $\rho_v(T)$ from our RCE simulations at various T_s, with both linear and log scales. These profiles are T_s-invariant in the sense that $\rho_v(T)$ does not depend on T_s—that is, that the ρ_v profiles at different T_s collapse onto a single curve.

For wavelengths λ where water vapor dominates, the optical depth τ_λ is just

$$\tau_\lambda(z) = \kappa(\lambda)\int_z^\infty \rho_v(z')\,dz', \qquad [3]$$

where $\kappa(\lambda)$ is a mass absorption coefficient (units m^2/kg) whose pressure-broadening and temperature-scaling we neglect (as in ref. 11; see also *SI Appendix*, text 2). Optical depth can be interpreted as minus the logarithm of the transmission function $e^{-\tau_\lambda(z)}$, which gives the fraction of radiation emitted at a given height that travels unabsorbed out to space. Changing variables in Eq. **3** to temperature yields

$$\tau_\lambda(T) \approx \kappa(\lambda)\int_{T_{tp}}^{T} \rho_v(T')\,\frac{dT'}{\Gamma}, \qquad [4]$$

where we neglect stratospheric water vapor and take the lower limit of the integral to be the tropopause temperature $T_{tp} \approx 185$ K, where radiative cooling goes to 0 (see Fig. 2, which also shows that T_{tp} is T_s-invariant). The only quantity in Eq. **4** that might still exhibit some T_s dependence is the lapse rate $\Gamma \equiv -\frac{dT}{dz}$, but figure 2 of ref. 11 shows that for moist adiabats typical of the tropics, $\Gamma(T)$ is also fairly T_s-invariant. [For GCMs, the presence of $\Gamma(T)$ in Eq. **4** will be more significant; see *Applicability to GCMs*.] Eq. **4** then implies that τ_λ profiles at any λ exhibit the same T_s invariance as ρ_v. This argument was also made by ref. 11, and its essence goes back to ref. 10. We check its validity with a line-by-line radiative transfer calculation in *SI Appendix*, Fig. S5.

To build on this and connect it with radiative cooling, we invoke the cooling-to-space approximation (24, 25), which says that the spectrally resolved LW flux divergence in temperature coordinates $-\partial_T F_\lambda^{LW}$ (units $W/m^2/K/m$, fluxes positive upward, minus sign introduced for consistent sign with $\partial_z F_\lambda^{LW}$) is approximately

$$-\partial_T F_\lambda^{LW} \approx \pi B_\lambda(T)\, e^{-\tau_\lambda(T)}\frac{d\tau_\lambda}{dT}. \qquad [5]$$

(Note that RRTM does not use Eq. **5**; we simply use it here as a heuristic.) Since the Planck function $B_\lambda(T)$ is T_s-invariant, as is the optical depth, we also expect $-\partial_T F_\lambda^{LW}$ to be T_s-invariant.

A similar argument holds for the SW flux divergence. If I_λ is the incident solar flux at wavelength λ and neglecting reflection and scattering in the near-infrared, then we have

$$-\partial_T F_\lambda^{SW} = -I_\lambda\, e^{-\tau_\lambda(T)}\frac{d\tau_\lambda}{dT} \qquad [6]$$

(ref. 24, equation 9.26). This equation is similar to Eq. **5** but with $B_\lambda(T)$ replaced by I_λ, and since I_λ is also T_s-invariant, $-\partial_T F_\lambda^{SW}$ should be also.

Since the above arguments hold for all wavelengths λ where water vapor dominates, and since such wavelengths comprise most of the LW and near-infrared SW bands, then we expect the spectrally integrated net (SW + LW) flux divergence $-\partial_T F^{net}$ ($W/m^2/K$) to also be T_s-invariant. This is confirmed in Fig. 2, which plots $(-\partial_T F^{net})(T)$ as diagnosed from RRTM coupled to our RCE simulations. That figure also plots $-\partial_T F^{net}$ as functions of z and p to emphasize that T_s invariance only holds when T is used as the vertical coordinate. *SI Appendix*, Figs. S2 and S3 show that this T_s invariance holds separately for the LW and SW.

Note that the fluxes in Fig. 2 are all-sky fluxes (which include cloud radiative effects), whereas the foregoing arguments were for clear skies. This is permissible because the clear-sky radiation dominates in our RCE simulations (*SI Appendix*, Fig. S4),

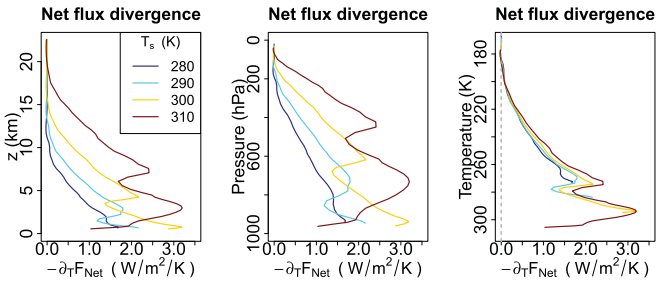

Fig. 2. Net flux divergence $-\partial_T F^{net}$, as diagnosed from RRTM coupled to our CRM RCE simulations at T_s = (280, 290, 300, 310) K. Fluxes are plotted from the lifting condensation level (LCL) of each simulation to 22.5 km for clarity and in height, pressure, and temperature coordinates to emphasize the T_s invariance of $(-\partial_T F^{net})(T)$. The gray dotted line (*Right*) plots $-\partial_T F^{net} = 0$ and shows the T_s invariance of $T_{tp} \approx 185$ K.

presumably due to the low cloud fraction (whose vertical maximum at the anvil height never exceeds $\sim 10\%$). It is also possible that the T_s invariance demonstrated here benefits from the fixed temperature of the anvil cloud peak (FAT) (26–28). We will touch upon cloud radiative effects further in section 5, when we apply these results to GCMs.

A Simple Picture for Column-Integrated Radiative Cooling

Now that we have established the T_s invariance of radiative flux divergences, we can construct a simple, quantitative picture of how column-integrated radiative cooling, and hence precipitation, changes with surface temperature.

Let F denote radiative flux in a particular band—LW, SW, or Net (LW + SW)–and Q the associated column-integrated free-tropospheric radiative cooling. (If these quantities appear in a statement with no subscript specifying a band, then the statement is meant to hold for all bands.) We consider the free troposphere (i.e., the troposphere above the planetary boundary layer), rather than the full troposphere, because the radiative constraint on precipitation

$$LP \approx Q_{\rm net} \qquad [7]$$

holds best for the free troposphere (1). The underlying assumption in Eq. **7** is that surface sensible heat fluxes balance radiative cooling in the boundary layer, and so both can be eliminated from the atmospheric energy budget by considering the free troposphere. (This assumption was also made in ref. 9 and goes back to ref. 29.) We define the free troposphere here as being above the lifting condensation level (LCL) $T_{\rm LCL}$ where clouds begin to form and below the tropopause $T_{\rm tp}$.

We now write Q as an integral of $-\partial_T F$ in temperature coordinates:

$$Q = \int_{T_{\rm tp}}^{T_{\rm LCL}} (-\partial_{T'} F)\, dT' \,.$$

If we approximate the change in $T_{\rm LCL}$ as equal to the change in T_s (this holds to within 10% in our CRM simulations), then the change in Q with surface temperature is simply

$$\frac{dQ}{dT_s} = -\partial_T F|_{T_{\rm LCL}}. \qquad [8]$$

In other words, since the tropospheric cooling profile $(-\partial_T F)(T)$ is independent of T_s, increasing T_s just exposes more of this profile. The contribution of this new section of the $(-\partial_T F)(T)$ curve to Q is given by Eq. **8**. A cartoon of this argument is given in Fig. 3. For finite changes in T_s, Eq. **8** approximates $(-\partial_T F)(T)$ in the newly exposed region as equal to $-\partial_T F$ at the LCL of the base state, but for small enough changes in T_s, this approximation should be adequate. Specializing Eq. **8** to the Net band and invoking Eq. **7** then yields an equation for precipitation change with surface warming. Note that Eq. **8** is predictive in the sense that only data from a single simulation are required for its evaluation.

Let us then test the predictive power of Eq. **8**. The panels of Fig. 4 plot $Q(T_s)$ as diagnosed directly from our CRM simulations, along with estimates of the slope of this curve diagnosed via Eq. **8**, for the SW, LW, and Net bands ($T_{\rm LCL}$ is diagnosed as T at the low-level maximum in cloud fraction). Precipitation LP is also plotted alongside $Q_{\rm net}$. Fig. 4 shows that Eq. **8** captures the changes in cooling in all bands. Furthermore, since LP tracks $Q_{\rm net}$ closely for $290 \le T_s \le 310$ K, Eq. **8** also captures precipitation changes in this temperature regime.

We also see that Eq. **8** predicts a decrease in $Q_{\rm net}$ with T_s at T_s = 320 K; this is not an artifact but rather a real effect due to the fact that $-\partial_T F^{\rm LW}$ tends toward zero with increasing T while $-\partial_T F^{\rm SW}$ stays roughly constant (*SI Appendix*, Figs. S2 and S3). That $-\partial_T F^{\rm LW}$ approaches zero indicates that all LW frequencies are becoming saturated—that is, $\tau_\lambda(T_s) > 1$ for all λ. This is the well-known "runaway greenhouse regime" (30), known to set in at roughly 310 K in the absence of large-scale circulations (31), as we have here, and at somewhat higher temperatures for GCMs (32, 33).

Note that our constraint Eq. **7** appears to break down in this T_s regime. This is due to the cooling of the atmosphere by raindrops that absorb heat as they fall to warmer temperatures, an effect that exceeds 10 W/m^2 in the T_s = 320 K case. This is not accounted for in Eq. **7** and also implies that Eq. **8** will slightly underpredict precipitation change at high T_s. The radiative constraint also breaks down at low T_s (i.e., $T_s \le 280$ K), where sensible heat fluxes start to dominate over latent heat fluxes. Thus, Eq. **8** has explanatory power for precipitation changes at temperatures somewhat greater than or equal to Earth's mean temperature of 288 K. Outside the $290 \le T_s \le 310$ K range, additional physics must be invoked to predict changes in P.

Why Does Precipitation Increase at $2-3\%$ K^{-1}?

The results in Fig. 4 show that our framework has some predictive power for explaining changes in $Q_{\rm net}$ and hence P in RCE. Let us then try to use this framework to answer the question posed in the introduction—namely, why does mean precipitation increase at $2-3\%$ K^{-1}?

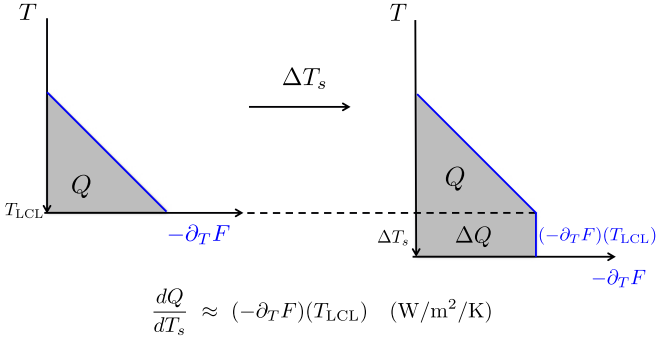

Fig. 3. Cartoon depicting the increase in Q with T_s in Eq. **8**. Increasing the temperature range of the troposphere exposes more of the T_s-invariant curve $(\partial_T F)(T)$ (blue lines). The contribution of this newly exposed region to column-integrated cooling is given by Eq. **8**.

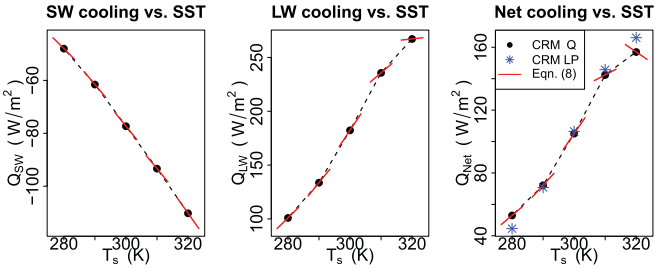

Fig. 4. Free-tropospheric radiative cooling Q vs. T_s (black circles), along with slopes dQ/dT_s (red lines) as diagnosed from Eq. **8**. These are shown for the SW (*Left*), LW (*Center*), and Net (*Right*) bands. The black dashed lines connect the black circles and give a benchmark slope against which to compare the red lines. The Net panel also gives CRM-diagnosed precipitation values in blue stars. See *A Simple Picture for Column-Integrated Radiative Cooling* for discussion.

First, let us confirm in a back-of-the-envelope fashion that Eq. **8** indeed gives a $2-3\%\ \mathrm{K}^{-1}$ increase in P. Combining Eqs. **7** and **8** gives

$$\frac{d\ln P}{dT_s} \approx \frac{(-\partial_T F^{\mathrm{net}})(T_{\mathrm{LCL}})}{Q_{\mathrm{net}}}. \qquad [9]$$

For $T_s = 300$ K, where $(-\partial_T F^{\mathrm{net}})(T_{\mathrm{LCL}}) \approx 3\ \mathrm{W/m^2/K}$ and $Q_{\mathrm{net}} = 104\ \mathrm{W/m^2}$, we find $\frac{d\ln P}{dT_s} = 3\%\ \mathrm{K}^{-1}$, as expected. This is also, of course, consistent with the directly diagnosed value of $\ln\left(\frac{P(310\ \mathrm{K})}{P(300\ \mathrm{K})}\right)/10\ \mathrm{K} = 3.14\%\ \mathrm{K}^{-1}$.

Now, suppose we take $T_s = 300$ K and try to simply parametrize the net cooling as $-\partial_T F^{\mathrm{net}} \propto (T - T_{\mathrm{tp}})^{\beta}$. Further suppose (motivated by inspection of Fig. 2) that $\beta \approx 2$—that is, that $-\partial_T F^{\mathrm{net}}$ is roughly quadratic in $(T - T_{\mathrm{tp}})$. Then, the full tropospheric radiative cooling is $Q \sim (T_s - T_{\mathrm{tp}})^{\beta+1}$, and hence

$$\frac{d\ln Q}{dT_s} = \frac{\beta+1}{T_s - T_{\mathrm{tp}}}. \qquad [10]$$

Note that $T_s - T_{\mathrm{tp}}$ is the depth of the troposphere expressed in temperature coordinates. For $T_s = 300$ K, this depth is roughly 100 K, and so Eq. **10** gives roughly $3\%\ \mathrm{K}^{-1}$, consistent with the result from Eq. **9**.

On the other hand, if $-\partial_T F^{\mathrm{net}}$ were constant throughout the depth of the troposphere (i.e., $\beta = 0$), then Q would just scale with $T_s - T_{\mathrm{tp}}$. But then it is clear that since a 1 K increase in T_s is a 1% increase in tropospheric depth $T_s - T_{\mathrm{tp}}$, Q should increase at $1\%\ \mathrm{K}^{-1}$, just as expected from Eq. **10**. The fact that Q increases somewhat faster than $1\%\ \mathrm{K}^{-1}$ can then be understood as a result of the fact that $-\partial_T F^{\mathrm{net}}$ is increasing, not constant, with T—that is, that $\beta > 0$ in Eq. **10**. In other words, Eq. **10** implies that the order of magnitude of fractional mean precipitation change is set by the increasing depth of the atmosphere $T_s - T_{\mathrm{tp}}$, which increases at $O(1\%)\ \mathrm{K}^{-1}$.

Applicability to GCMs

Now we apply the ideas developed so far to GCM simulations. Given the complexity of GCMs, we do not aim for the same quantitative agreement as found in the CRM case but rather to show that the same basic ideas allow us to make an order of magnitude estimate for how Q and P change with warming in GCMs. In particular, we do not aim to capture any of the intermodel scatter in these changes.

The key so far has been the T_s invariance of $-\partial_T F$. We can check this in a GCM by binning GCM columns by their local T_s, computing an average $-\partial_T F$ profile for each bin, and then checking the T_s invariance of each of these profiles. For this, we utilize the AMIP (Atmospheric Model Intercomparison Project) and AMIP4K output in the CMIP5 (Climate Model Intercomparison Project Phase 5) archive. These experiments are atmosphere-only and feature observed sea-surface temperatures (AMIP) as well as uniform +4K perturbations to those observed sea-surface temperatures (AMIP4K), with no change in CO_2 concentration; as such, they are good analogs to our fixed-T_s CRM experiments. The AMIP4K experiment was part of the CFMIP protocol (Cloud Feedback Model Intercomparison Project) (34), which also requested the output of vertically resolved radiative fluxes rather than just surface and top-of-atmosphere fluxes, allowing us to compute $-\partial_T F$ profiles.

Six models participated in the AMIP and AMIP4K CFMIP experiments and provided the output we require. We begin by analyzing the first one whose data we obtained, IPSL-CM5A-LR (Institute Pierre Simon Laplace Coupled Model 5A Low Resolution). Fig. 5 shows AMIP and AMIP4K profiles of average $-\partial_T F^{\mathrm{net}}$ for six of our T_s bins, where for each T_s bin the average is taken over all columns from the last 30 y of the simulation for which the lowest model-level air temperature lies in the range $(T_s, T_s + 2\mathrm{K})$. For the AMIP4K calculation in each panel, the $T_s + 4\mathrm{K}$ bin is used, so as to compare roughly the same columns between the two simulations. See *Materials and Methods* for further details.

Fig. 5 shows that for IPSL-CM5A-LR and a given T_s, T_s invariance hold throughout most of the troposphere, with the profiles diverging at some point in the lower troposphere, below which the AMIP4K profile typically shifts downward by about 4 K relative to the AMIP profile. We interpret this downward shift as the influence of various surface-based atmospheric layers (e.g., subcloud layer, trade cumulus layer) on our profiles, as the surface and hence the tops of such layers are not expected to stay fixed in T with warming. Fig. 6 shows that this behavior is fairly robust across our CFMIP models.

To connect this behavior with that of our RCE simulations, note that Eq. **8** is equivalent to assuming that the $-\partial_T F^{\mathrm{net}}$ profile for a climate with surface temperature $T_s + \Delta T_s$ may be obtained from the $-\partial_T F^{\mathrm{net}}$ profile for a climate with surface temperature T_s by inserting, at T_{LCL}, a vertical segment of length ΔT_s and magnitude $(-\partial_T F^{\mathrm{net}})(T_{\mathrm{LCL}})$. Under such an extension procedure, it is clear that Eq. **8** holds. We now attempt the same approach for each of our GCM's T_s bins; that is, we attempt to construct, from each AMIP $-\partial_T F^{\mathrm{net}}$ profile,

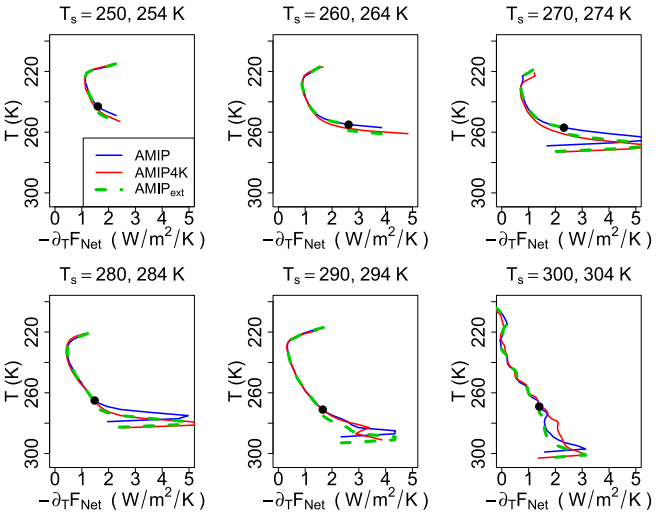

Fig. 5. Profiles of $-\partial_T F^{\mathrm{net}}$ for various T_s bins for the AMIP (blue) and AMIP4K (red) runs of IPSL-CM5A-LR, along with the AMIP$_{ext}$ profiles (green dashed) produced by extension of the AMIP profiles at T_{ext} (black dots; see *Applicability to GCMs* for description). The AMIP$_{ext}$ profiles are overall a decent match to the AMIP4K profiles.

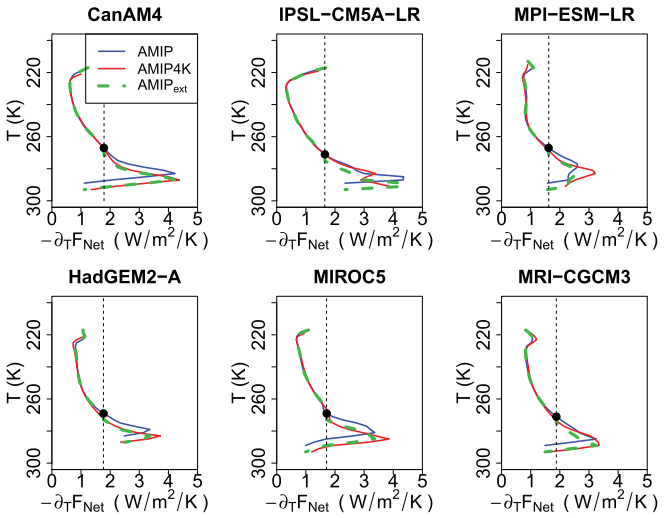

Fig. 6. As in Fig. 5, but for the T_s = 290 K (AMIP) and 294 K (AMIP4K) bins for all six CFMIP models. The AMIP_{ext} profiles are again a decent match to the AMIP4K profiles, and their values $-\partial_T F^{\text{net}}(T_{\text{ext}}) \lesssim 2\ \text{W/m}^2/K$ at the insertion point T_{ext} roughly approximate the actual global dQ/dT_s values (see *Applicability to GCMs*).

an extended AMIP_{ext} profile that matches the AMIP4K profile. The issue then is how to determine the extension point T_{ext} where the vertical segment of length ΔT_s should be inserted. This should be the average within each T_s bin of where the free troposphere begins, but unlike for the CRM, the physics that sets this level varies in time and space, complicating a direct diagnosis on physical grounds. Below this level, however, we expect that $\Gamma(T)$ profiles within a T_s bin will vary much more than in the free troposphere, due to variations in the depth and strength of stable layers and the absence of gravity waves in convective boundary layers (*SI Appendix*, Fig. S6). By Eqs. **4** and **5**, $-\partial_T F^{\text{net}} \sim 1/\Gamma$, and so this low-level pickup in variance in $\Gamma(T)$ implies a similar pickup in variance in $-\partial_T F^{\text{net}}$ (*SI Appendix*, Fig. S7). We thus determine T_{ext} for a given T_s bin as the T where the variance of $(-\partial_T F^{\text{net}})(T)$ within that bin exceeds a certain fixed threshold (*SI Appendix*, 2.1 and Fig. S7; black dots in Figs. 5 and 6).

With T_{ext} in hand, we then construct AMIP_{ext} profiles as described above and superimpose them on the AMIP and AMIP4K profiles of Figs. 5 and 6, demonstrating that AMIP_{ext} profiles can be a decent match to the AMIP4K profiles. Furthermore, in the $T_s = 290,\ 294$ K bins of Fig. 6 (closely corresponding to the global mean T_s in the AMIP and AMIP4K simulations), the vertical dashed lines mark $(-\partial_T F^{\text{net}})(T_{\text{ext}})$, which we see is somewhat less than 2 $\text{W/m}^2/\text{K}$ for each model. This is in the neighborhood of the actual value of $dQ/dT_s = 2.4 \pm 0.4\ \text{W/m}^2/\text{K}$ (mean ± 1 SD across our CFMIP model ensemble, corresponding to percentage increases of $2.3 \pm 0.3\%\ \text{K}^{-1}$), demonstrating a plausible connection between our formalism and the behavior of these comprehensive GCMs. Although in some cases the AMIP_{ext} profile is not a very good fit to the AMIP4K profile (e.g., the IPSL panel in Fig. 6), examination of other T_s bins (*SI Appendix*, Fig. S8) shows that this is the exception rather than the rule.

Summary and Discussion

We summarize our findings as follows:

- Radiative cooling profiles in temperature coordinates in RCE are T_s-invariant (Fig. 2), yielding simple models for how Q and P change with T_s (Eqs. **8** and **10**).
- These simple models capture the simulated changes (Fig. 4) and also suggest that the order-of-magnitude of precipitation changes are governed by tropospheric depth, which increases at $O(1\%)\ \text{K}^{-1}$.
- For T_s-binned $-\partial_T F$ profiles from AMIP GCM simulations, a procedure equivalent to that for the CRM yields rough estimates of dQ/dT_s close to 2 $\text{W/m}^2/\text{K}$, broadly consistent with AMIP4K simulations.

This work could be further developed in many ways. One next step would be to better understand these surface-based layers, which are deeper for larger T_s (*SI Appendix*, Figs. S6 and S7), and how they influence $-\partial_T F$ profiles. *SI Appendix*, Figs. S9 and S10 show that some lower tropospheric features in the $-\partial_T F^{\text{net}}$ profiles are due to cloud-radiative effects. *SI Appendix*, Fig. S11 shows that relative humidity profiles, when binned as for $-\partial_T F^{\text{net}}$, exhibit a similar T_s invariance aloft (in line with the CRM results of ref. 20) but also have features that shift down near the surface (see also ref. 35). With a better understanding of these features, one could refine our order-of-magnitude estimates for the GCMs into a more quantitative estimate capable of predicting intermodel scatter.

There are also unanswered questions regarding the argument given in T_s *Invariance of Flux Divergences*. For instance, what are the conditions for the cooling-to-space approximation in Eq. **5** to be valid? Note that ref. 25, which is the standard reference, demonstrates the validity of the approximation empirically but not theoretically. Also, why does the radiative tropopause temperature T_{tp} appear to be fixed in our simulations? This bears a certain resemblance to FAT but is distinct from it, as the radiative tropopause and anvil peak are distinct features of the atmosphere and occur at quite different heights (approximately 17 km and 11 km, respectively, in our T_s = 300 K RCE simulation).

There is also the question of robustness of our RCE results to choice of CRM. Uncertainties in subgrid turbulence and microphysics schemes can lead to substantial uncertainties in cloud cover (36, 37), potentially affecting the T_s invariance exhibited here. The upcoming RCE Model Intercomparison Project (RCEMIP) (38) would make an ideal venue for investigating this.

Finally, Eq. **10** encapsulates the point made by refs. 2–4 and many others that the scaling of Q_{net} and P with T_s need not resemble the canonical $7\%\ \text{K}^{-1}$ Clausius–Clapeyron (CC) scaling of $p_v^*(T)$. The CC and mean precipitation scalings are independent constraints with different physical origins, the former purely thermodynamic and the latter largely radiative. That they are independent and may thus be combined without circularity is what makes them powerful, allowing for, for example, a prediction of how convective mass fluxes change with warming (6).

Materials and Methods

We here describe in detail our calculation of bin-averaged flux divergence profiles from GCM output. Note that all data used in constructing all of the figures presented here can be found at https://github.com/jeevanje/rad_cooling.

For a GCM column at a given longitude, latitude, and time (we use monthly mean output), we must first identify a range of tropospheric model levels k over which the temperature T varies monotonically. We identify the uppermost of these levels k_{max} as the minimum $k > 10$ for which $T[k+1] > T[k]$. If none such exists (i.e., no stratospheric inversion), then k_{max} takes its highest possible value (i.e., model top). The minimum k value k_{min} equals 1 if there is no inversion below k_{max} and otherwise is the largest $k < k_{\text{max}}$ such that $T[k] > T[k-1]$. We then interpolate the column's SW and LW radiative fluxes over this T range onto a uniform T grid running from 150 to 350 K in increments of 2 K and assign these interpolated profiles, weighted by column area, to the appropriate T_s bin using $T[1]$ (where T_s binning is done with the same uniform grid as for vertical levels T). We repeat this for each GCM column over the last 30 y of each simulation, keeping track of the accumulated column area for each bin and T level. This allows us to produce an area-weighted average flux profile in each bin, where in

a given bin the total area represented at each T level drops off at lower and higher T (due to small variations in $T[k_{\min}]$ and $T[k_{\max}]$ within the bin). These average flux profiles (one per bin) may then be differentiated with respect to T, yielding the $-\partial_T F^{\text{net}}$ profiles shown in Figs. 5 and 6. To reduce artifacts from binning, the profiles are cut off once the total area at a given T is less than 90% of the maximum value in the vertical (where this maximum value is taken throughout most of that bin's tropospheric T range, as expected).

The decomposition of these net flux divergence profiles into their LW and SW components is given in *SI Appendix*, Fig. S12, which shows that T_s invariance aloft holds for the LW and SW separately in the GCMs, just as for the CRM.

ACKNOWLEDGMENTS. We thank Tim Merlis, Mark Cane, Jake Seeley, David Paynter, Yi Ming, and Leo Donner for helpful comments during various stages of this work; to Mark Zelinka, Robert Pincus, and Tim Cronin for encouragement; and to the patient reviewers and editor of this work for their close reading and thoughtful comments. This work was supported by the US Department of Energy (DOE)'s Atmospheric System Research, an Office of Science, Office of Biological and Environmental Research program; Lawrence Berkeley National Laboratory and its National Energy Research Scientific Computing Center (which provided computing resources) are operated for the DOE by the University of California under Contract DE-AC02-05CH11231. N.J. was supported by the Princeton Atmosphere and Ocean Sciences Visiting Scientist Program and a Harry Hess fellowship from the Princeton Geosciences Department.

1. O'Gorman PA, Allan RP, Byrne MP, Previdi M (2012) Energetic constraints on precipitation under climate change. *Surv Geophys* 33:585–608.
2. Allen MR, Ingram WJ (2002) Constraints on future changes in climate and the hydrologic cycle. *Nature* 419:224–232.
3. Mitchell JFB, Wilson CA, Cunnington WM (1987) On CO_2 climate sensitivity and model dependence of results. *Q J R Meteorol Soc* 113:293–322.
4. Stephens GL, Ellis TD (2008) Controls of global-mean precipitation increases in global warming. *J Clim* 21:6141–6155.
5. Lambert FH, Webb MJ (2008) Dependency of global mean precipitation on surface temperature. *Geophys Res Lett* 35:1–5.
6. Held IM, Soden BJ (2006) Robust responses of the hydrological cycle to global warming. *J Clim* 19:5686–5699.
7. Stephens GL, Hu Y (2010) Are climate-related changes to the character of global-mean precipitation predictable? *Environ Res Lett* 5:025209.
8. Pendergrass AG, Hartmann DL (2014) The atmospheric energy constraint on global-mean precipitation change. *J Clim* 27:757–768.
9. Takahashi K (2009) Radiative constraints on the hydrological cycle in an idealized radiative-convective equilibrium model. *J Atmos Sci* 66:77–91.
10. Simpson G (1928) Some studies in terrestrial radiation. *Mem R Meteorol Soc* 2:69–95.
11. Ingram WJ (2010) A very simple model for the water vapour feedback on climate change. *Q J R Meteorol Soc* 136:30–40.
12. Romps DM (2011) Response of tropical precipitation to global warming. *J Atmos Sci* 68:123–138.
13. Muller CJ, O'Gorman PA, Back LE (2011) Intensification of precipitation extremes with warming in a cloud-resolving model. *J Clim* 24:2784–2800.
14. Romps DM (2008) The dry-entropy budget of a moist atmosphere. *J Atmos Sci* 65:3779–3799.
15. Mlawer EJ, Taubman SJ, Brown PD, Iacono MJ, Clough SA (1997) Radiative transfer for inhomogeneous atmospheres: RRTM, a validated correlated-k model for the longwave. *J Geophys Res* 102:16663.
16. Lin YL, Farley RD, Orville HD (1983) Bulk parameterization of the snow field in a cloud model. *J Clim Appl Meteorol* 22:1065–1092.
17. Lord SJ, Willoughby HE, Piotrowicz JM (1984) Role of a parameterized ice-phase microphysics in an axisymmetric, nonhydrostatic tropical cyclone model. *J Atmos Sci* 41:2836–2848.
18. Krueger SK, Fu Q, Liou KN, Chin HNS (1995) Improvements of an ice-phase microphysics parameterization for use in numerical simulations of tropical convection. *J Appl Meteorol* 34:281–287.
19. Margolin LG, Rider WJ, Grinstein FF (2006) Modeling turbulent flow with implicit LES. *J Turbulence* 7:N15.
20. Romps DM (2014) An analytical model for tropical relative humidity. *J Clim* 27:7432–7449.
21. Wing AA, Emanuel K, Holloway CE, Muller C (2017) Convective self-aggregation in numerical simulations: A review. *Surv Geophys* 38:1173–1197.
22. Fläschner D, Mauritsen T, Stevens B (2016) Understanding the inter-model spread in global-mean hydrological sensitivity. *J Clim* 29:801–817.
23. Samset BH, et al. (2017) Weak hydrological sensitivity to temperature change over land, independent of climate forcing. *npj Clim Atmos Sci* 1:1–8.
24. Thomas GE, Stamnes K (2002) *Radiative Transfer in the Atmosphere and Ocean* (Cambridge Univ Press, Cambridge, UK), p 517.
25. Rodgers CD, Walshaw CD (1966) The computation of infra-red cooling rate in planetary atmospheres. *Q J R Meteorol Soc* 92:67–92.
26. Hartmann DL, Larson K (2002) An important constraint on tropical cloud-climate feedback. *Geophys Res Lett* 29:12-1–12-4.
27. Kuang Z, Hartmann DL (2007) Testing the fixed anvil temperature hypothesis in a cloud-resolving model. *J Clim* 20:2051–2057.
28. Harrop BE, Hartmann DL (2012) Testing the role of radiation in determining tropical cloud-top temperature. *J Clim* 25:5731–5747.
29. Betts AK, Ridgway W (1989) Climatic equilibrium of the atmospheric convective boundary layer over a tropical ocean. *J Atmos Sci* 46:2621–2641.
30. Pierrehumbert RT (2010) *Principles of Planetary Climate* (Cambridge Univ Press, Cambridge, UK).
31. Goldblatt C, Robinson TD, Zahnle KJ, Crisp D (2013) Low simulated radiation limit for runaway greenhouse climates. *Nat Geosci* 6:661–667.
32. Wolf E, Toon E (2014) Delayed onset of runaway and moist greenhouse climates for Earth. *Geophys Res Lett* 41:167–172.
33. Leconte J, Forget F, Charnay B, Wordsworth R, Pottier A (2013) Increased insolation threshold for runaway greenhouse processes on Earth-like planets. *Nature* 504:268–271.
34. Bony S, et al. (2011) CFMIP: Towards a better evaluation and understanding of clouds and cloud feedbacks in CMIP5 models. *Clivar Exch* 16:20–24.
35. Cronin TW, Wing AA (2017) Clouds, circulation, and climate sensitivity in a radiative-convective equilibrium channel model. *J Adv Model Earth Syst* 9:2883–2905.
36. Tsushima Y, et al. (2015) High cloud increase in a perturbed SST experiment with a global nonhydrostatic model including explicit convective processes. *J Adv Model Earth Syst* 6:571–585.
37. Igel AL, Igel MR, van den Heever SC (2014) Make it a double: Sobering results from simulations using single-moment microphysics schemes. *J Atmos Sci* 72:910–925.
38. Wing AA, Satoh M, Reed KA, Stevens B, Bony S (2017) Radiative-convective equilibrium model Intercomparison Project. *Geosci Model Dev Discuss* 11:1–24.